Nanoscale

PAPER

View Article Online
View Journal | View Issue

Cite this: *Nanoscale*, 2022, **14**, 11187

Ag@Pd bimetallic structures for enhanced electrocatalytic CO_2 conversion to CO: an interplay between the strain effect and ligand effect†

Zuolong Chen, Xiyang Wang, Lei Wang and Yimin A. Wu *

Received 3rd June 2022,
Accepted 15th July 2022

DOI: 10.1039/d2nr03079a

rsc.li/nanoscale

Electrochemical CO_2 reduction reactions provide a promising path to effectively convert CO_2 into valuable chemicals and fuels for industries. Among the many CO_2 conversion catalysts, Pd stands out as a promising catalyst for effective CO_2 to CO conversion. Here, using the misfit strain strategy, Ag@Pd bimetallic nanoparticles with different Pd overlayer contents were prepared as CO_2 reduction catalysts. By varying the Pd overlayer content, all the Ag@Pd bimetallic nanoparticles exhibited superior CO_2 conversion performance over their Pd and Ag nanoparticle counterparts. An optimal Pd-to-Ag ratio of 1.5 : 1 yielded the highest CO faradaic efficiency of 94.3% at −0.65 V *vs.* RHE with a high CO specific current density of 3.9 mA cm^{-2}. It was found that the Pd content can substantially affect the interplay between the strain effect and ligand effect, resulting in optimized binding properties of the reaction intermediates on the catalyst surface, thereby enhancing the CO_2 reduction performance.

Introduction

The historically unprecedented global CO_2 emission levels and the resulting global warming have imposed high risks and devastating damages on the modern world, with projected extreme weather events and species extinction.[1] Moreover, in our industrialized and overly populated world, increasing energy demand has posed another challenge to human society in the 21st century. Unfortunately, the conventional energy generation model, where a large amount of fossil fuels are consumed every year to produce both energy and CO_2, has been one of the major CO_2 emission sources since the industrial revolution.[2] To date, numerous strategies have been developed to meet the growing energy demand and deal with global warming by converting CO_2 into fuels and chemicals *via* thermochemical, photochemical, and electrochemical approaches.[3] In these strategies, the electrochemical CO_2 reduction reaction (CO_2RR), which utilizes electrochemical electrolyzers and catalysts to reduce CO_2 to various products, has demonstrated many unique advantages, such as tunable reaction parameters, high conversion performance, and mild work environment.[4] While the electrochemical CO_2 conversion to multi-carbon products is still limited by low conversion efficiency and complex reaction paths, electrochemical CO_2 reduction to CO has gained much attention due to its high conversion efficiency and more economically viable nature.[5,6]

The development of electrochemical CO_2 conversion demands the advancement of high-performance catalysts. Among the many optimization strategies, bimetallic structures and strain engineering have recently emerged as effective strategies to enhance catalytic performance by altering the electronic structures of catalysts.[7–10] Bimetallic nanoparticles often create strains due to lattice mismatch between the two components.[11] Nørskov *et al.* proposed that strain can change the overlapping of orbitals in transition metal atoms and thus change the width of their d-band.[12] A narrowed band induced by tensile strain can upshift the d-band center to a higher energy level and strengthen chemisorption by decreasing the electron density in the antibonding states, resulting in improved reactant–catalyst interactions, thus affecting the overall reaction activity.[11] Utilizing the misfit strain that arises from the difference in the lattice parameters between two materials has been a major approach for creating strained catalysts.[9,11,13] The strain can be easily engineered in such structures by utilizing the strain relaxation phenomenon. The strain created at the substrate–overlayer interface can be quickly released as the overlayer grows thicker with higher overlayer contents.[13,14] Strain engineering has yielded exciting catalytic performance in various CO_2RR systems, and it was found that tensile strain could enhance the CO_2 to CO conversion efficiency.[15,16] Nevertheless, when two dissimilar metals

Department of Mechanical and Mechatronics Engineering, Waterloo Institute for Nanotechnology, Materials Interfaces Foundry, University of Waterloo, Waterloo, Ontario N2L 3G1, Canada. E-mail: yimin.wu@uwaterloo.ca

† Electronic supplementary information (ESI) available. See DOI: https://doi.org/10.1039/d2nr03079a

are employed to create misfit strain, the ligand effect can play a crucial role in such systems. Electronic charge transfers can occur between two dissimilar surface metal atoms, thus affecting their electronic structures and creating the so-called ligand effect.[17] Therefore, the ligand effect can also affect the overall catalytic performance of strained structures by shifting the d-band center, and it needs to be considered when studying strain-engineered catalyst systems.[18,19]

Herein, Ag@Pd nanoparticles with different Pd contents are studied to probe the CO_2RR performance of bimetallic catalysts and study the effect of Pd content. Ag@Pd bimetallic structures were fabricated through a step-growth synthesis method to control the Pd-to-Ag ratios and therefore vary the strain profiles by relaxing the misfit strain originating from the Ag–Pd interface. It was found that an optimal Pd overlayer content can yield an optimized interplay between the tensile strain effect and the ligand effect, thus promoting the CO_2 to CO conversion reactions, resulting in enhanced CO conversion performance. Remarkably, a high CO faradaic efficiency (FE) of 94.8% was achieved with Ag@Pd nanoparticles with a Pd-to-Ag ratio of 1.5. This configuration yielded excellent stability by maintaining a CO FE of over 90% in a 12-hour test and over 85% in a 22-hour test with a slight drop in the current density. However, higher Pd content yields inferior CO_2RR performance due to more relaxed strain and, therefore, a less pronounced strain effect. On the other hand, the ligand effect is more effective in the Ag@$Pd_{0.75}$ sample, which has the lowest Pd content, resulting in weakened COOH adsorption. Electrochemical characterization proved that a balanced interplay between the strain and ligand effects along with the preferred adsorption sites of key intermediates can result in the desired adsorption behaviors of intermediates, suggesting a promising bimetallic catalyst system for electrochemical CO_2 to CO conversion.

Results and discussion

Ag@Pd bimetallic nanoparticles with different Pd-to-Ag ratios were synthesized and named after their Pd-to-Ag molar ratios. Ag@$Pd_{0.75}$ samples have the lowest Pd content, with a Pd-to-Ag molar ratio of 0.75. Ag@$Pd_{1.5}$ has a Pd-to-Ag ratio of 1.5, and the same naming principle applies to Ag@Pd_3 samples.

Fig. 1a shows the HAADF-STEM image of the Ag@Pd1.5 Ag@Pd nanoparticles. Due to the low *Z* contrast between Ag and Pd (the atomic numbers of Ag is 47 and Pd is 46) and because the Pd overlayer is too thin in such structures, the Pd layers can not be easily identified through the *Z* contrast in STEM images.[20,21] The HAADF-STEM image was then false-colored based on the contrast intensity using the equalized mode with the DigitalMicrograph software. As shown in Fig. 1b, the boundary between green and orange can help identify the Ag–Pd interface, where the dark green layers represent the thin Pd overlayers on the Ag surface (marked by orange and red). It can be estimated that there are approximately 2 to 3 Pd overlayers.

To better measure the interplanar spacing and determine the interface, the red box region in Fig. 1c was processed through fast Fourier transform (FFT) and then through inverse Fourier transform (IFFT) to reconstruct the image, as shown in Fig. 1d.[22] Fig. 1d reveals a clear interface with distortions/edge dislocations between the two sets of lattice fringes, proving lattice misfit between the two components. In addition, the location of the interface matches that in the false-colored image (Fig. 1b). As shown in Fig. 1e and f, on the two sides of the interface, the line profiles of two locations marked in green (corresponding to the outer part) and red (corresponding to the inner part) were measured for interplanar spacing. The *d*-spacing of atoms in the green area is about 2.304 Å, showing Pd (111) with a tensile strain of approximately 2.6%. A *d*-spacing of 2.329 Å is measured on the inner side of the interface, corresponding to a compressively strained (−1.27%) Ag (111) plane. It can also be estimated that there are about 2 to 3 layers of Pd grown on the surface of Ag. However, due to the difficulty of characterizing the *d* spacing in the outmost layers of spherical nanoparticles and the strain relaxation effect, the Pd strain profile characterized here shall not be assumed to be the same as the strain profile in the outmost layer, which is catalytically active in the CO_2 to CO conversion reactions. Hence, we will focus on the effect of Pd content in the Ag@Pd structures, while knowing that a higher overlayer content shall result in thicker overlayers with less strain.[11,13,23] In addition, electron energy loss spectroscopy (EELS) mapping was conducted for the elemental analysis of the Ag–Pd nanoparticles. As shown in Fig. 1g–i, the center of the nanoparticle is mainly Ag, which is surrounded by a very thin Pd layer (marked with green). In the overlay image, it can see that Pd element is not evenly distributed over the outer layer of Ag in the 2D project (Fig. 1i). Some of the Pd coverage on top of the Ag along the zone axis also exists. This is because EELS is a sensitive characterization technique that can capture the weak signals from the surface Pd layer, which may only consist of a few layers of Pd atoms in the 3D sphere. The additional STEM images of other Ag@Pd nanoparticles are presented in Fig. S1.†

To further characterize the Ag@Pd nanoparticles with different Pd content, Fig. 2 shows grazing angle X-ray diffraction (GIXRD) patterns of Ag@$Pd_{0.75}$, Ag@$Pd_{1.5}$, and Ag@Pd_3 nanoparticles. GIXRD is a surface-sensitive characterization with low sample penetration depth that can characterize small nanoparticles with thin overlayers. However, the small nanoparticle sizes (which can yield severe peak broadening), close diffraction peaks between Ag and Pd, and thin Pd overlayers collectively resulted in convoluted GIXRD diffraction peaks. Meanwhile, the deconvolution of the XRD patterns in the core–shell structures has been reported as an effective approach for analyzing the strain profiles.[13,24] Hence, by deconvoluting the GIXRD peaks, it was found that the Pd(111) peaks in all the Ag@Pd samples shift toward lower angles, indicating larger *d*-spacings and tensile strains in the Pd overlayers. A lower Pd content in Ag@Pd structures reveals a more negative shift and hence larger tensile strain. The Pd(111)

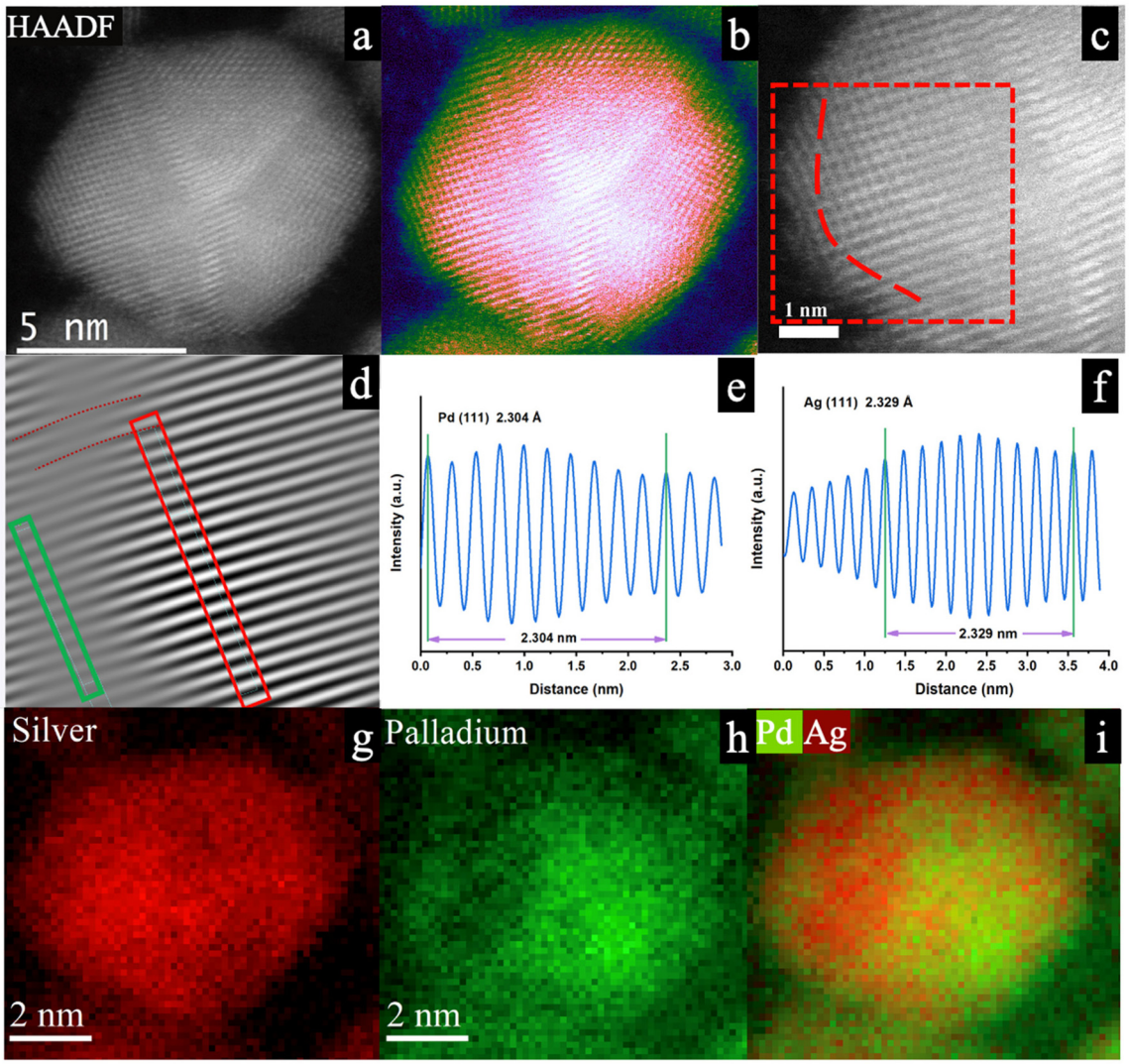

Fig. 1 (a) HAADF-STEM images of the Ag@$Pd_{1.5}$ nanoparticles; (b) false-colored HAADF-STEM images; (c) and (d) Ag–Pd boundary and the reconstructed images from Fourier transform; (e) and (f) the profile of the highlighted area in (d); (g), (h) and (i) EELS elemental analyses for Ag, Pd, and the overlay image.

peak of Ag@$Pd_{0.75}$ is located at about 39.35°, suggesting an expanded *d* spacing of approximately 2.291 Å and tensile strain of 2%. On the other hand, the Ag(111) peaks in all the Ag@Pd samples are located at about 38.5°, exhibiting a positive shift from the Ag reference peak and compressive strain on Ag. The shifts in both the Ag and Pd GIXRD peaks can confirm strained Ag–Pd interfaces. In addition, when the Pd-to-Ag ratio increases from 0.75 to 1.5, the intensity of Pd characters in the convoluted peaks becomes more dominant as it evolves from a weak peak in the Ag@$Pd_{0.75}$ sample to a more intense peak in the Ag@Pd_3 samples. After integrating the area under the Ag and Pd peaks, it was found that the ratio of the Pd peak area to the Ag peak area (Pd : Ag) evolved from 0.79 in Ag@$Pd_{0.75}$ to 3.98 in Ag@Pd_3. Similarly, the Ag(200) peak at about 44.5° gradually diminishes with higher Pd ratios in the Ag@Pd structures as thicker Pd overlayers result in less X-ray interaction with the Ag underlayer. The Ag(200) peak can be seen in the GIXRD patterns due to the random orientations of nanoparticles during the GIXRD test. As the Pd overlayers get thicker, the Ag(200) peak gets weaker. Note that, as estimated from the HAADF images, the *d* spacing of the Pd layer close to the Ag–Pd boundary is about 2.304 Å in Ag@$Pd_{1.5}$ (Fig. 1d and e). This discrepancy between these two measurements is due to the limited resolution in the XRD characterization and the peak deconvolution of the assembling measurement, but STEM measures the very localized parameter in individual nanoparticles. In addition, the XRD characterization of nanoparticles is subject to the size effect, and the XRD spectra only show the average lattice parameters of all the nanoparticles in the measured sample.[14,25] Consequently, such GIXRD peak locations shall only be used to detect and estimate the tensile strain amplitude rather than to quantify the

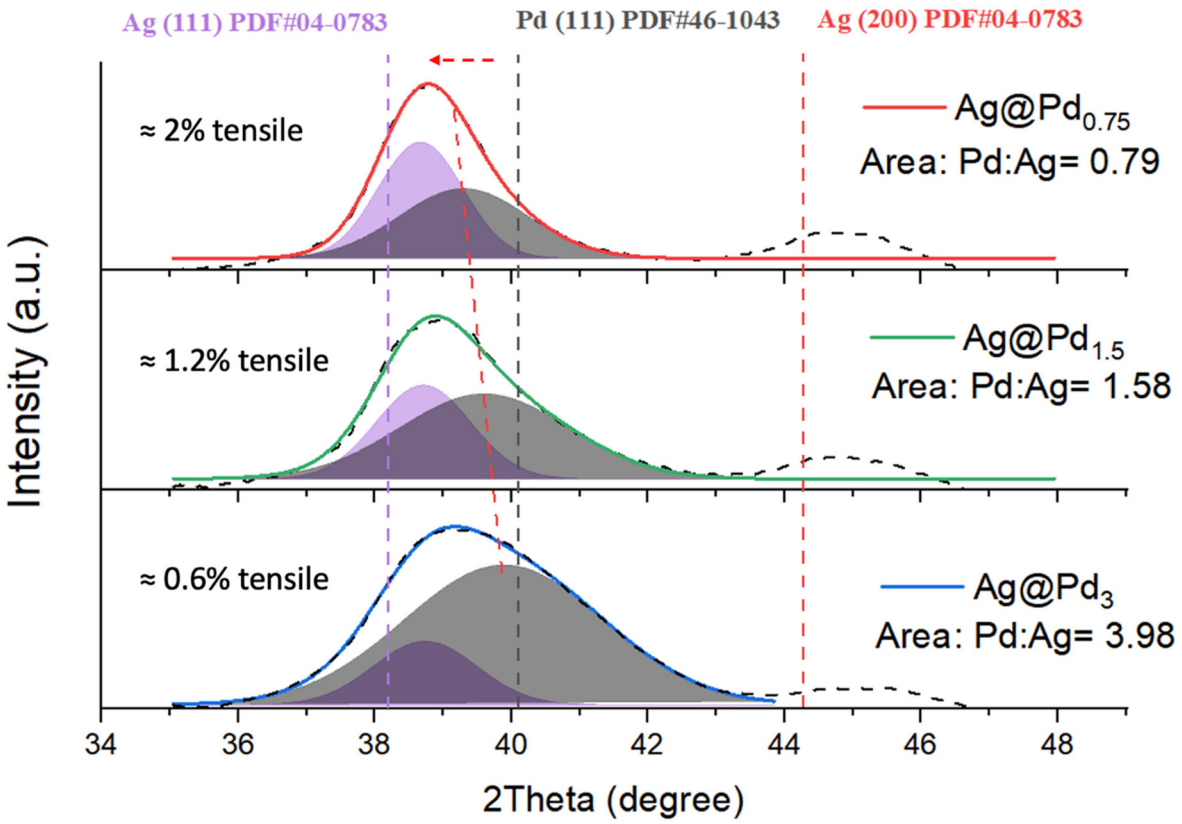

Fig. 2 The original (black dashes) and deconvoluted GIXRD patterns of the Ag@Pd nanoparticles.

strain precisely. Nevertheless, the HAADF STEM images and GIXRD data can confirm the tensile strain in Ag@Pd nanoparticles and that a lower Pd content ($Ag@Pd_{0.75}$) can yield a higher tensile strain.

The XPS spectra of all the Ag@Pd samples are shown in Fig. S2.† The XPS survey of all the Ag@Pd samples confirms the presence of both Pd and Ag elements in the nanoparticles. Moreover, the atomic percentage of Pd and Ag elements estimated by the signal intensities can prove the Pd coverage on Ag. In the $Ag@Pd_{0.75}$ sample, even though Pd has a molar ratio of 45% in the Ag@Pd structures, the surface-sensitive XPS signals estimate a higher Pd percentage of 53.82%. This is because the Pd overlayer hinders the photo-excited electron transfer from the Ag sublayer to the vacuum. Thus, the Ag percentage is underestimated by XPS. Further, the XPS peaks were deconvoluted to compare the peak locations of the Pd 3d and Ag 3d orbitals.

In Fig. 3a, the Pd 3d spectra can be deconvoluted into two peaks. The more intense peaks at lower binding energies denote Pd at a zero-valent state, while the weaker peaks at slightly higher binding energies correspond to oxidized Pd.[26] Oxidation might occur due to air exposure before XPS characterization. All the Ag@Pd samples show negative shifts in the Pd 3d binding energy peaks, and larger shifts are associated with Ag@Pd structures with lower Pd contents. Notably, at a peak position of 334.5 eV, the binding energy of the Pd $3d_{5/2}$ state in $Ag@Pd_{0.75}$ sample shifts −0.7 eV compared with pure Pd nanoparticles, and the Pd $3d_{3/2}$ state experienced a comparable negative shift of −0.71 eV. In the $Ag@Pd_3$ sample with the highest Pd content, the peak shift is still significant at a value of −0.25 eV. Both the strain and ligand effect can decrease the binding energy.[27] When Pd atoms experience tensile strains, the interatomic distance increases, thus reducing the overlap of the d orbitals and narrowing the bandwidth. The narrowed d-band can bring up the d-band center close to the Fermi level and destabilize the d-electrons, making it easier to ionize the metal and decrease the binding energy.[27] The upshifted d band center can strengthen the adsorption of key reaction intermediates and promote catalytic reactions.[11,12] However, because of the ligand effect, Ag can transfer electrons to the Pd overlayer and increase the electron density, therefore decreasing the binding energy of Pd 3d orbitals and lowering the d-band center in Pd.[7,18] Indeed, as shown in Fig. 3b, the Ag 3d peaks in Ag@Pd bimetallic structures all shift toward lower binding energies, indicating an electron-poor state of Ag due to the electron transfer from Ag to Pd.[28] Consequently, the lowest Pd 3d binding energy of $Ag@Pd_{0.75}$ implies the most powerful ligand effect among all the Ag@Pd samples. To summarize, the GIXRD and XPS data together suggest the largest strain and ligand effect on the $Ag@Pd_{0.75}$ surface.

The catalytic performance of Ag@Pd structures with different Pd content was evaluated. Overall, the CO faradaic

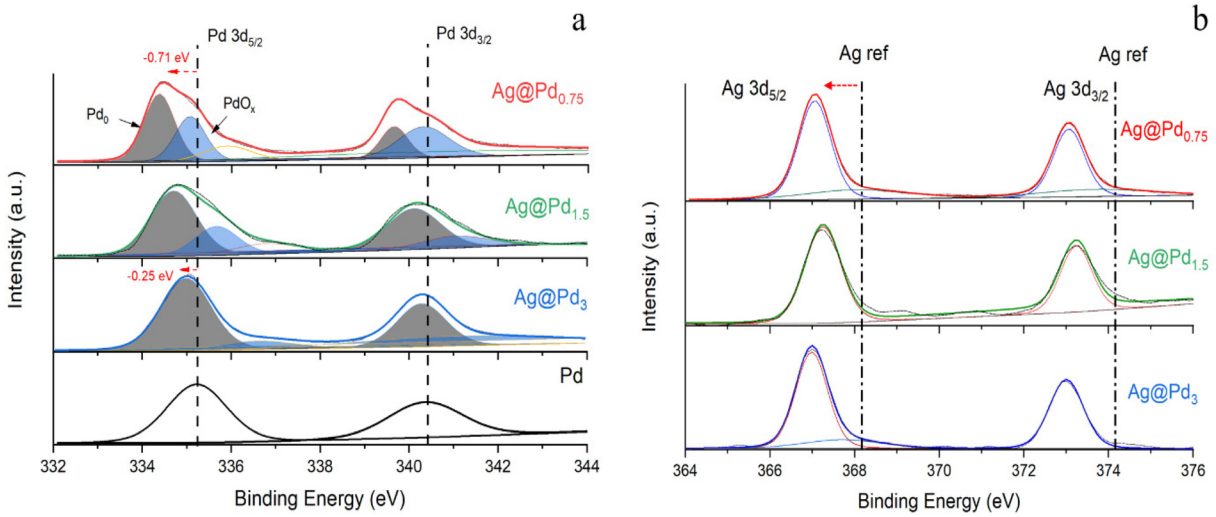

Fig. 3 XPS spectra of Ag@Pd nanoparticles with different Pd contents: (a) Pd 3d spectra and (b) Ag 3d spectra.

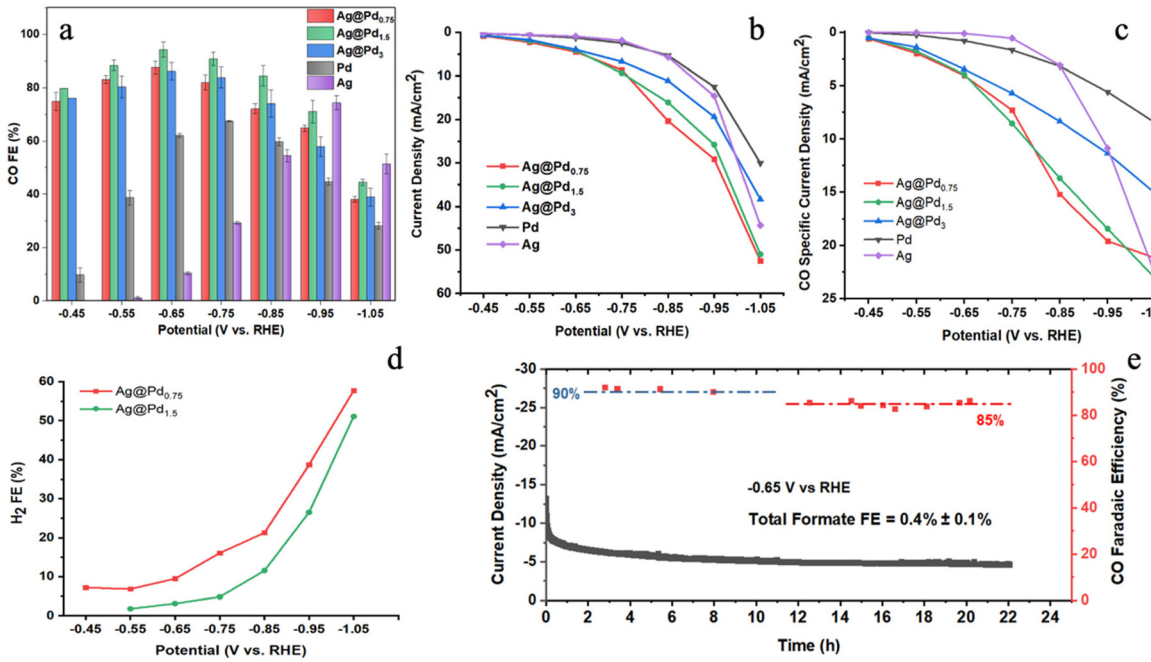

Fig. 4 (a) CO faradaic efficiency (FE) of different Ag@Pd nanoparticles; (b) and (c) overall current densities and CO specific current densities of Ag@Pd nanoparticles; (d) H_2 FE comparison between $Ag@Pd_{0.75}$ and $Ag@Pd_{1.5}$; (e) current density and CO FE of $Ag@Pd_{1.5}$ in the long-term stability test.

efficiencies of Ag@Pd structures all demonstrated enhanced performance over pure Ag and Pd nanoparticles. A remarkable CO FE of 94.3% was achieved with the $Ag@Pd_{1.5}$ bimetallic nanoparticle (Fig. 4a), which has an intermediate Pd content among all Ag@Pd structures. At the optimal potential of −0.65 V, formate is the primary liquid product with a faradaic efficiency of about 4%. Fig. S3† shows the NMR spectrum of the liquid sample after the 22-hour long-term stability test. Compared with the Ag@Pd bimetallic structures with thinner and thicker Pd overlayers (lower or higher Pd content), $Ag@Pd_{1.5}$ outperformed the control samples at all the potentials. Even at a lower potential of −0.55 V RHE, the $Ag@Pd_{1.5}$ sample achieved a high FE of over 88%. In terms of the current density, which is an indicator of the activity of catalysts, all Ag@Pd structures showed higher activities than pure Pd nanoparticles (Fig. 4b). The $Ag@Pd_3$ sample, with its highest Pd content, demonstrated the lowest activity among all the Ag@Pd structures (Fig. 4b). As a result of the above per-

formance, the CO specific current density, an indicator of the specific activity for CO conversion, also shows that the Ag@Pd structures all outperformed pure Pd and Ag nanoparticles (Fig. 4c). The difference in the CO specific current density between $Ag@Pd_{0.75}$ and $Ag@Pd_{1.5}$ is not as significant as that between $Ag@Pd_3$ and any of these two samples. The increase in the CO specific current densities is more pronounced compared with pure Pd and Ag control samples. $Ag@Pd_{0.75}$ showed a higher current density than $Ag@Pd_{1.5}$. Hence, the CO specific current density is slightly higher than that of $Ag@Pd_{1.5}$. Among the best two catalysts, $Ag@Pd_{0.75}$ and $Ag@Pd_{1.5}$, the higher current density of $Ag@Pd_{0.75}$ might be attributed to the more robust H_2 evolution reaction (HER) on its surface, as shown in Fig. 4d, where a higher H_2 FE was achieved on $Ag@Pd_{0.75}$ than on $Ag@Pd_{1.5}$, making $Ag@Pd_{0.75}$ an inferior catalyst for the CO_2 to CO conversion reaction. The long-term stability of the $Ag@Pd_{1.5}$ sample was also tested in the same H-Cell setup for 22 hours without replenishing the electrolyte (Fig. 4e). A minor decrease in the current density was observed after four hours of testing, while the CO FE remained well above 90% (Fig. 4e). After 20 hours of testing, the FE still achieved a high value of about 85%. The current density experienced a mild drop in the first 8 hours but stabilized afterward, showing excellent long-term stability of the catalysts (Fig. 4e).

To investigate the enhancement mechanism of Ag@Pd structures with different Pd-to-Ag ratios, a series of electrochemical characterization was conducted to investigate the adsorption and desorption behaviors of key reaction intermediates on both the Ag@Pd structures and control samples (Pd and Ag nanoparticles). The electrochemical reduction of CO_2 to CO involves three key steps:

$$CO_{2(g)} + H_{(aq)}{}^{+} + e^{-} + * \rightarrow COOH* \quad (1)$$

$$COOH* + H_{(aq)}{}^{+} + e^{-} \rightarrow CO* + H_2O_{(l)} \quad (2)$$

$$CO* \rightarrow CO_g + * \quad (3)$$

where * refers to a catalytically active site on the surface that can adsorb reaction species. COOH* and CO* are the adsorbed COOH and CO, respectively. It has been proven through both theoretical and experimental studies that step (1) is the rate-limiting step, especially on the Pd(111) surface.[16,29,30] In addition, in step (2), the conversion from COOH* to CO* is facile.[29] Hence, the binding strength of COOH* is critical in this process, and stronger COOH* adsorption can result in enhanced CO_2 to CO conversion efficiency.[16] The adsorption of CO_2 and COOH on the Pd surface can both be investigated through the adsorption of hydroxyl, which has been employed as an alternative in the characterization.[16,31–33] Moreover, surface hydroxyls have been proposed to offer active sites to enhance CO_2 adsorption *via* hydrogen bonds.[34] Thus, the subsequent formation of COOH* can be promoted. Both the above mechanisms justify the correlation between the adsorption of hydroxyl and the formation of COOH*. Hence, the adsorption of hydroxyl on Ag@Pd catalysts was investigated by characterizing the reduction of $Pd(OH)_2$ in cyclic voltammetry (CV) tests.

To investigate the COOH and H_2 adsorption behaviors on all the catalysts, Fig. 5a and c show the whole CV scans of all the Ag@Pd structures and the control samples in Ar-saturated 0.1 M NaOH and Ar-saturated 0.1 M $HClO_4$, respectively. The current was normalized by the reaction surface area and expressed as the current density. As revealed in Fig. 5a, the oxidative scans show that the Ag oxidation peak at about 0.75 V *vs.* RHE is not observed in all the Ag@Pd samples. Similarly, in the reductive scans of all the Ag@Pd samples, there is no reduction peak at about 0.57 V, which corresponds to the Ag^+ reduction peak.[35] The absence of Ag oxidation and reduction peaks in the CV scans of Ag@Pd structures suggests that there is no considerable Ag exposure on the surface of the Ag@Pd samples. More importantly, by zooming in on the $Pd(OH)_2$ reduction potential range between 0.45 V and 0.85 V in Fig. 5a, Fig. 5b shows shifts in such reduction potentials in the Ag@Pd samples. Notably, compared with pure Pd, all Ag@Pd samples exhibit more negative reduction potentials in the cathodic scan, indicating higher barriers for reducing $Pd(OH)_2$ and a higher OH coverage (as more electrons were needed), thus stronger adsorption of OH on the Pd overlayers. The adsorption of OH is probed as an alternative of the adsorption of CO_2 and COOH in this test; thus, the more negative reduction potential suggests stronger CO_2 and COOH adsorptions on all the Ag@Pd samples.[16,32] With its most negative peak at 0.675 V *vs.* RHE, $Ag@Pd_{1.5}$ reveals the most active CO_2 and COOH adsorption site. $Ag@Pd_{0.75}$ shows a more positive $Pd(OH)_2$ reduction peak at 0.688 V (Fig. 5b), even with the lowest Pd content and the largest tensile strain (as evidenced by GIXRD in Fig. 2). Due to the more relaxed strain with a higher Pd content, $Ag@Pd_3$ shows a most positive peak location among all the Ag@Pd samples, suggesting the lowest CO_2 adsorption strength, thus resulting in lower CO FE and current density. The CV scans conducted in the Ar-saturated 0.1 M $HClO_4$ electrolyte also exhibit the same trend in Fig. 5c. By zooming in on the 0–0.6 V *vs.* RHE range in Fig. 5c, Fig. 5d can help study the hydrogen adsorption behaviors. Among all the Ag@Pd samples, $Ag@Pd_{0.75}$ exhibits a more positive and sharper hydrogen adsorption peak at 0.15 V *vs.* RHE. In comparison, the H adsorption peak on $Ag@Pd_{1.5}$ shifted by −15 mV. This observation suggests that $Ag@Pd_{0.75}$ provides a stronger H adsorption site than $Ag@Pd_{1.5}$.[36] We then focus on the comparison between $Ag@Pd_{0.75}$ and $Ag@Pd_{1.5}$ as they have the best CO_2 conversion performance in terms of the CO FE at the optimal potential range (−0.65 V *vs.* RHE) and the highest current densities. Interestingly, the electrochemical catalysis studies reveal that the lowest Pd content and the largest tensile strain (as proven by the GIXRD) in $Ag@Pd_{0.75}$ does not lead to a higher CO FE but a higher H_2 FE, as shown in Fig. 4a and d. Hence, the strongest ligand effect on $Ag@Pd_{0.75}$ (as revealed by XPS) shall play an important role. In fact, the interplay of the ligand effect and the strain effect in conjunction with the preferred adsorption sites of different key reactants determines the CO_2 conversion behaviors of Ag@Pd nanoparticles with

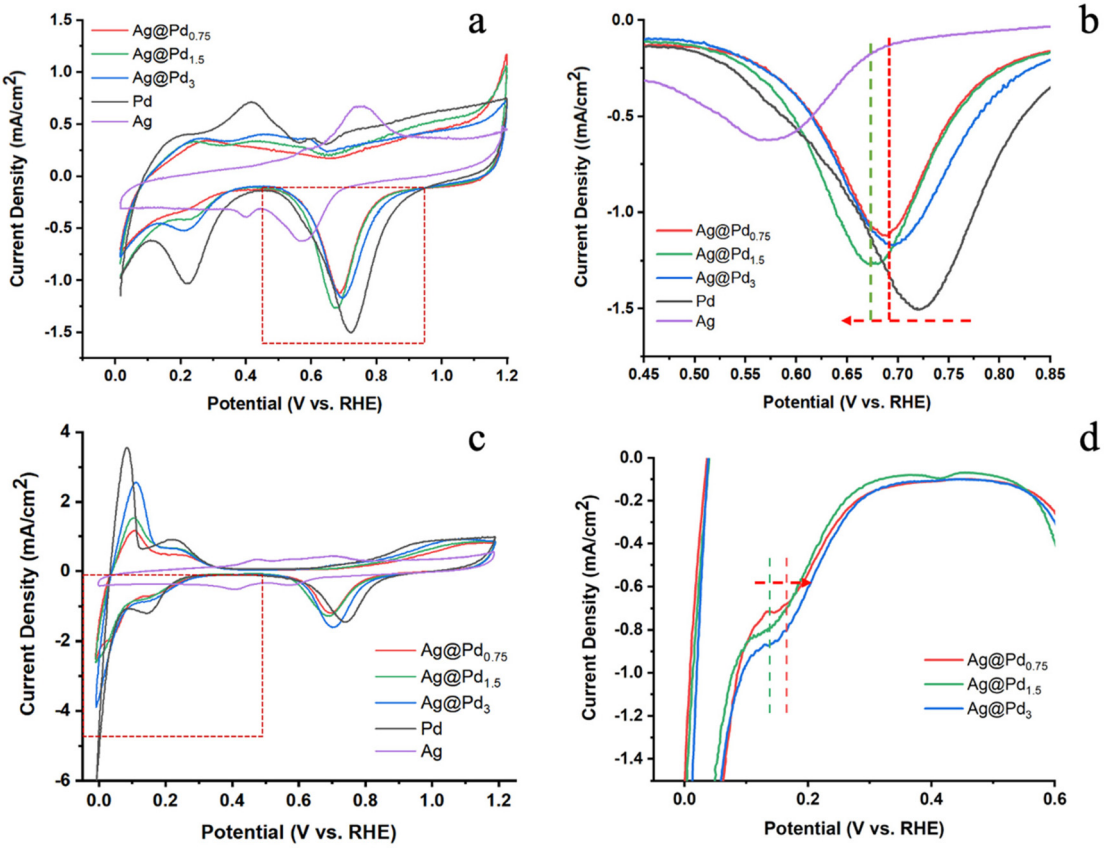

Fig. 5 (a) CV scan of Ag@Pd nanoparticles in a 0.1 M NaOH electrolyte; (b) the amplified area in (a); (c) CV scan of Ag@Pd nanoparticles in a 0.1 M $HClO_4$ electrolyte; (d) the amplified area in (c).

different Pd contents. Theoretical studies suggest that the ligand effect, which lowers the d band center due to the Pd–Ag interaction, and thus competes against the strain effect and dominates the strain effect with one Pd monolayer grown on Ag.[18] Similar findings have also been reported with other bimetallic systems but with different numbers of monolayers.[11] However, until the strain is fully relaxed, the strain effect becomes more pronounced with more Pd layers (higher Pd content) on Ag; thus, the interplay between the ligand effect and the strain effect results in enhanced adsorption of the reaction intermediates. Meanwhile, theoretical calculation predicts that the ligand effect plays a more decisive role on the top site of Pd atoms, where HCOO and HCO prefer to adsorb, and that the influence of the ligand effect on the hollow site, where CO and H tend to adsorb, is less significant.[18] Hence, the decreased COOH adsorption strength on the $Ag@Pd_{0.75}$ catalyst, as indicated by the more positive position of the Pd $(OH)_2$ reduction peak (Fig. 5b), can be attributed to the more effective ligand effect with the lowest Pd content. In contrast, the higher Pd content in the $Ag@Pd_{1.5}$ nanoparticles can attenuate the impact of the ligand effect while maintaining strong tensile strain, as characterized by GIXRD. Hence, the strain effect becomes dominant and enhances the COOH adsorption. Another possible contributor to the enhanced COOH adsorption on $Ag@Pd_{1.5}$ is the second-layer effect. It suggests that when the highly directional bonding orbitals between the adsorbate and the first layer of atoms are perpendicular to the surface, the bonding orbitals can overlap with the second layer atoms and further enhance the adsorption energies––this is the case for intermediates absorbed on the top sites.[37] This second-layer effect and other similar enhancing mechanisms in bimetallic systems have been studied and proven in previous studies.[18,37–40] As a result, step (1) in the overall reaction will be promoted. On the other hand, the ligand effect (which can down-shift the d band and lower the adsorption strength) is less effective on the hollow site, where H and CO prefer to adsorb. As shown in Fig. 5d, the stronger H adsorption on $Ag@Pd_{0.75}$ suggests that the strain effect is more dominant for the adsorption of H. Hence, the H_2 FE is significantly higher with $Ag@Pd_{0.75}$ than $Ag@Pd_{1.5}$. HER is a competitive reaction against the CO_2 reduction reaction.[41] Therefore, $Ag@Pd_{0.75}$ showed inferior CO_2 reduction performance in terms of the CO FE.[42] Moreover, the CO adsorption behaviors were investigated through the CO stripping experiment. As shown in Fig. S4,† the CO oxidation potential on the $Ag@Pd_{0.75}$ surface (0.963 V *vs.* RHE) is higher than that on the $Ag@Pd_{1.5}$ surface (0.945 V *vs.* RHE), suggesting a slightly higher CO oxidation barrier and thus stronger CO binding on

the $Ag@Pd_{0.75}$ surface. This finding is in agreement with the discussion above. In summary, the asymmetric modification of the adsorption behaviors of different reactants, COOH, H, and CO, is a combined consequence of the following factors: (a) the interplay of the ligand effect and strain effect, (b) different intermediates prefer different adsorption sites (top sites *vs.* hollow sites), and (c) the second-layer effect that further enhances the adsorption of intermediates absorbed on the top sites.[18] In addition, even though the desorption of CO is not the rate-determining step over Pd(111), the CO coverage on the Pd surface can still affect the adsorption of COOH due to adsorbate–adsorbate interactions.[30] As a result of all the above mechanisms, the strengthened CO_2 and COOH adsorption and the weakened H and CO adsorption over the $Ag@Pd_{1.5}$ together culminated in a high CO FE of 94.3% with Ag@Pd bimetallic structures with an optimal Pd content.

Conclusion

We have demonstrated that an optimal Pd content in Ag@Pd bimetallic nanoparticles can enhance the CO_2 conversion performance on Ag@Pd catalysts through the interplay between strain and ligand effects. With a Pd-to-Ag ratio of 1.5, $Ag@Pd_{1.5}$ structures yielded a remarkable CO faradaic efficiency of 94.3% and demonstrated a stable conversion performance over 22 hours. It is proposed that an optimal Pd content can benefit from the synergistic effect of strain engineering and the second-layer effect, thus substantially promoting the COOH adsorption, which is the rate-determining step in the CO_2 to CO conversion reaction over the Pd(111) surface. With a lower Pd content, even though the strain showed a maximum, the ligand effect becomes more dominant and can weaken the COOH adsorption on the top sites. In contrast, the adsorptions of CO and H are not substantially weakened as they prefer to adsorb on the hollow sites. On the other extreme, as seen in the case of $Ag@Pd_3$, a much higher Pd content can induce more strain relaxation. Hence, the enhancement for COOH adsorption is attenuated. This work demonstrated a highly effective, strain-engineered CO_2RR catalyst for CO_2 to CO conversion. In addition, it provides more experimental evidence to the state of knowledge of strain-engineered catalysts and further proves that a suitable overlayer content is crucial for maximizing the strain effect while inhibiting the undesired ligand effect in misfit strain systems.

Experimental

Materials

Palladium(II) nitrate hydrate ($Pd(NO_3)_2{\cdot}2H_2O$), silver nitrate ($AgNO_3$), potassium bicarbonate ($KHCO_3$), polyvinyl pyrrolidone (PVP), potassium hydroxide (KOH), acetone, and ethanol were purchased from Sigma-Aldrich. Ethylene glycol was purchased from VWR Chemicals. Argon and CO_2 were provided by Linde Gas. Ultrapure water (18 MΩ cm) was used in all experiments.

Synthesis of Ag@Pd nanoparticles

A 2-step reduction method was used to synthesize Ag@Pd bimetallic nanoparticles.[20,21] For the synthesis of $Ag@Pd_{1.5}$ nanoparticles, first, 120 mg of PVP was completely dissolved in 30 mL of ethylene glycol under vigorous stirring in a round bottom flask. Then, 0.225 mmol of $AgNO_3$ was completely dissolved into the above solution, and the homogeneous solution was slowly heated to 120 °C under argon protection. After maintaining a growth temperature of 120 °C for 30 min, the flask was quenched in cold water. A PVP–Ag nanoparticle colloid with yellow color is formed in this way. A 30 mL ethylene glycol solution containing 0.338 mmol of $Pd(NO_3)_2{\cdot}2H_2O$ was added to the Ag NP colloid for the sequential reduction. Next, the homogeneous solution was heated to 90 °C and maintained at 90 °C for 120 min under argon protection. The resulting Ag@Pd nanoparticles were then precipitated with an excessive amount of acetone and washed five times with water, ethanol, and acetone. Ag@Pd nanoparticles with other Pd-to-Ag ratios were synthesized *via* the same method but with different amounts of Pd according to the desired molar ratios. Pd nanoparticles were prepared *via* the same procedure at 90 °C, but $Pd(NO_3)_2{\cdot}2H_2O$ was used in the first step instead of $AgNO_3$. Afterward, two sequential reductions were conducted with $Pd(NO_3)_2{\cdot}2H_2O$ solutions of the same composition.

Structural and electronic characterizations

High-angle annular dark-field scanning transmission electron microscopy (HAADF-STEM) images were acquired by an FEI Titan 80–300 HB TEM at the Canadian Centre for Electron Microscopy. Grazing Incidence X-ray Diffraction (GIXRD) was characterized by a Panalytical MRD with a Cu source. The GIXRD optics include a parabolic W/Si mirror, slits on the source side, and a 0.27-degree parallel plate collimator on the detector side. X-ray photoelectron spectroscopy (XPS) measurements were conducted using a Thermo-VG Scientific ESCALab 250 Microprobe system equipped with a hemispherical analyzer and a monochromatic Al Kα X-ray source (1486.6 eV).

Electrochemical measurements

To prepare the catalyst ink, 2 mg of the prepared catalyst was dispersed in a solution that contained 490 μL of isopropanol and 10 μL of Nafion™ 117 (5%, Sigma-Aldrich). The mixture was then sonicated for 30 min for complete dispersion and consequently air-brushed on a piece of carbon paper with an active area of 2 cm^2 as the working electrode. The electrochemical measurements were conducted in an H-cell reactor with the Nafion™ 211 membrane separating the two half-cells at room temperature and under atmospheric pressure. The electrolytes for both the anode and cathode sides were 0.5 M $KHCO_3$ solutions. An Ag/AgCl reference electrode and Pt counter electrode were used with a CHI660 (Chenhua, Shanghai) electrochemical workstation. Before each test, the electrolyte was saturated with CO_2 for 30 min. The gas product was analyzed by an Agilent 6890 gas chromatograph (GC) equipped with a Carboxen® 1000 column and a CarbonPLOT

column for the flame ionization detector and thermal conductivity detector, respectively. The liquid products were measured with a Bruker 500 MHz Nuclear Magnetic Resonance (NMR) using an internal reference prepared with D_2O and DMSO.

All potentials reported in this study were measured against the Ag/AgCl reference electrode and converted to reversible hydrogen potential (RHE) using the equation below:

$$E\ (vs.\ \mathrm{RHE}) = E\ (vs.\ \mathrm{Ag/AgCl}) + 0.059 \times \mathrm{pH} + 0.197$$

Cyclic voltammetry (CV) was carried out in both 0.1 M NaOH and 0.1 M $HClO_4$ solutions under argon from 0 V to 1.2 V *vs.* RHE with a scan rate of 20 mV s^{-1}. The electrode was prepared with the same catalyst loading and had an area of 1 cm^2. The CO stripping experiment was conducted by polarizing the electrode at 0.2 V in a CO-saturated environment for 20 min and then an argon-saturated environment for 30 min while maintaining the same bias. Then, the CV scan was conducted three times from 0.2 V to 1.2 V at 20 mV s^{-1} to characterize the $Pd(OH)_2$ reduction peak and baseline. CV tests were conducted using a Gamry Reference 3000™ potentiostat.

Conflicts of interest

There are no conflicts to declare.

Acknowledgements

Y. A. W gratefully acknowledges the funding from the Natural Sciences and Engineering Research Council of Canada (NSERC) (RGPIN-2020-05903, GECR-2020-00476). Z. C gratefully acknowledges the financial support from NSERC Canadian Graduate Scholarship Doctoral Program. We also gratefully acknowledge Prof. John Z. Wen for providing the gas chromatography used in this study.

References

1 P. M. Cox, R. A. Betts, C. D. Jones, S. A. Spall and I. J. Totterdell, *Nature*, 2000, **408**, 184–187.
2 K. L. Denman, G. Brasseur, A. Chidthaisong, P. Ciais, P. M. Cox, R. E. Dickinson, D. Hauglustaine, C. Heinze, E. Holland, D. Jacob, U. Lohmann, S. Ramachandran, P. L. da Silva Dias, S. C. Wofsy and X. Zhang, Couplings Between Changes in the Climate System and Biogeochemistry, in *Climate Change 2007: The Physical Science Basis. Contribution of Working Group I to the Fourth Assessment Report of the Intergovernmental Panel on Climate Change*, ed. S. Solomon, D. Qin, M. Manning, Z. Chen, M. Marquis, K. B. Averyt, M. Tignor and H. L. Miller, Cambridge University Press, Cambridge, United Kingdom and New York, NY, USA, 2007.
3 S. C. Peter, *ACS Energy Lett.*, 2018, **3**, 1557–1561.
4 Z. Chen, X. Wang, J. P. Mills, C. Du, J. Kim, J. Z. Wen and Y. A. Wu, *Nanoscale*, 2021, **13**, 19712–19739.
5 S. Verma, B. Kim, H.-R. M. Jhong, S. Ma and P. J. A. Kenis, *ChemSusChem*, 2016, **9**, 1972–1979.
6 D. A. Salvatore, D. M. Weekes, J. He, K. E. Dettelbach, Y. C. Li, T. E. Mallouk and C. P. Berlinguette, *ACS Energy Lett.*, 2018, **3**, 149–154.
7 C. Li, S. Yan and J. Fang, *Small*, 2021, 2102244, DOI: 10.1002/smll.202102244.
8 T. Kim, R. E. Kumar, J. A. Brock, E. E. Fullerton and D. P. Fenning, *ACS Catal.*, 2021, **11**, 6662–6671.
9 R. P. Jansonius, L. M. Reid, C. N. Virca and C. P. Berlinguette, *Acs Energy Lett.*, 2019, **4**, 980–986.
10 M. K. Birhanu, M. C. Tsai, C. T. Chen, A. W. Kahsay, T. S. Zeleke, K. B. Ibrahim, C. J. Huang, Y. F. Liao, W. N. Su and B. J. Hwang, *Electrochim. Acta*, 2020, **356**, 10.
11 Z. Xia and S. Guo, *Chem. Soc. Rev.*, 2019, **48**, 3265–3278.
12 M. Mavrikakis, B. Hammer and J. K. Nørskov, *Phys. Rev. Lett.*, 1998, **81**, 2819–2822.
13 J. Zhao, B. Chen and F. Wang, *Adv. Mater.*, 2020, **32**, 2004142.
14 T. Jocelyn, A. Leonardi, X. Sang, K. M. Koczkur, R. R. Unocic, M. Engel and S. E. Skrabalak, *Nanoscale Adv.*, 2020, **2**, 1105–1114.
15 M. Du, X. Zhao, G. Zhu, H.-Y. Hsu and F. Liu, *J. Mater. Chem. A*, 2021, **9**, 4933–4944.
16 H. Huang, H. Jia, Z. Liu, P. Gao, J. Zhao, Z. Luo, J. Yang and J. Zeng, *Angew. Chem., Int. Ed.*, 2017, **56**, 3594–3598.
17 P. Strasser, S. Koh, T. Anniyev, J. Greeley, K. More, C. Yu, Z. Liu, S. Kaya, D. Nordlund, H. Ogasawara, M. F. Toney and A. Nilsson, *Nat. Chem.*, 2010, **2**, 454–460.
18 J. Cho, S. Lee, J. Han, S. P. Yoon, S. W. Nam, S. H. Choi, K.-Y. Lee and H. C. Ham, *J. Phys. Chem. C*, 2014, **118**, 22553–22560.
19 X. Yang, X. Tong, X. Liu, K. Li and N. Yang, *Electrochem. Commun.*, 2021, **123**, 106917.
20 K. Tedsree, T. Li, S. Jones, C. W. A. Chan, K. M. K. Yu, P. A. J. Bagot, E. A. Marquis, G. D. W. Smith and S. C. E. Tsang, *Nat. Nanotechnol.*, 2011, **6**, 302–307.
21 X. Li, Z. Zeng, B. Hu, L. Qian and X. Hong, *ChemCatChem*, 2017, **9**, 924–928.
22 H.-B. Wang, F. Ma, Q.-Q. Li, C.-Z. Dong, D.-Y. Ma, H.-T. Wang and K.-W. Xu, *Nanoscale*, 2013, **5**, 2857.
23 P. Wang, W. Nong, Y. Li, H. Cui and C. Wang, *Appl. Catal., B*, 2021, **288**, 119999.
24 J. Zhao, B. Chen, X. Chen, X. Zhang, T. Sun, D. Su and F. Wang, *Nanoscale*, 2020, **12**, 13973–13979.
25 A. V. Vorontsov and S. V. Tsybulya, *Ind. Eng. Chem. Res.*, 2018, **57**, 2526–2536.
26 R. Toyoshima, M. Yoshida, Y. Monya, Y. Kousa, K. Suzuki, H. Abe, B. S. Mun, K. Mase, K. Amemiya and H. Kondoh, *J. Phys. Chem. C*, 2012, **116**, 18691–18697.
27 D. Chen, C. Li, H. Liu, F. Ye and J. Yang, *Sci. Rep.*, 2015, **5**, 11949.
28 Y. Liu, R. G. Jordan and S. L. Qiu, *Phys. Rev. B: Condens. Matter Mater. Phys.*, 1994, **49**, 4478–4484.
29 H. A. Hansen, J. B. Varley, A. A. Peterson and J. K. Nørskov, *J. Phys. Chem. Lett.*, 2013, **4**, 388–392.

30 H. Liu, J. Liu and B. Yang, *Phys. Chem. Chem. Phys.*, 2020, **22**, 9600–9606.
31 A. Salehi-Khojin, H.-R. M. Jhong, B. A. Rosen, W. Zhu, S. Ma, P. J. A. Kenis and R. I. Masel, *J. Phys. Chem. C*, 2013, **117**, 1627–1632.
32 D. Gao, H. Zhou, J. Wang, S. Miao, F. Yang, G. Wang, J. Wang and X. Bao, *J. Am. Chem. Soc.*, 2015, **137**, 4288–4291.
33 S. Zhang, P. Kang and T. J. Meyer, *J. Am. Chem. Soc.*, 2014, **136**, 1734–1737.
34 W. Deng, L. Zhang, L. Li, S. Chen, C. Hu, Z. J. Zhao, T. Wang and J. Gong, *J. Am. Chem. Soc.*, 2019, **141**, 2911–2915.
35 M. Innocenti, C. Zafferoni, A. Lavacchi, L. Becucci, F. Di Benedetto, E. Carretti, F. Vizza and M. L. Foresti, *J. Electrochem. Soc.*, 2014, **161**, D3018–D3024.
36 Y. Zhu, M. Yuan, L. Deng, R. Ming, A. Zhang, M. Yang, B. Chai and Z. Ren, *RSC Adv.*, 2017, **7**, 1553–1560.
37 Y. Gohda and A. Groß, *J. Electroanal. Chem.*, 2007, **607**, 47–53.
38 Q. Xie, G. O. Larrazábal, M. Ma, I. Chorkendorff, B. Seger and J. Luo, *J. Energy Chem.*, 2021, **63**, 278–284.
39 S. Sultan, J. H. Kim, S. Kim, Y. Kwon and J. S. Lee, *J. Energy Chem.*, 2021, **60**, 410–416.
40 W. Dai, J. Long, L. Yang, S. Zhang, Y. Xu, X. Luo, J. Zou and S. Luo, *J. Energy Chem.*, 2021, **61**, 281–289.
41 Y.-J. Zhang, V. Sethuraman, R. Michalsky and A. A. Peterson, *ACS Catal.*, 2014, **4**, 3742–3748.
42 H. Xie, Y. Wan, X. Wang, J. Liang, G. Lu, T. Wang, G. Chai, N. M. Adli, C. Priest, Y. Huang, G. Wu and Q. Li, *Appl. Catal., B*, 2021, **289**, 119783.